Implementation of a Near-Wake Region within the Curled-Wake Model

Paul Hulsman[1], Luis A. Martínez-Tossas[2], Nicholas Hamilton[2], and Martin Kühn[1]

[1]ForWind – Institute of Physics, University of Oldenburg, Küpkersweg 70, 26129 Oldenburg, Germany

[2]National Wind Technology Center, National Renewable Energy Laboratory, Golden, CO, 80401, USA

Correspondence: Paul Hulsman, paul.hulsman@forwind.de

Abstract. Modelling the near-wake region becomes more important as turbines are positioned with a relatively smaller spacing due to site restrictions, leading to significant power losses and increased fatigue loading. These effects can be mitigated by actively steering the wake away from the downstream turbine. This paper presents an approach to analytically estimate the wake deficit within the near-wake region by modifying the curled wake model. This is done by incorporating a new initial

5 condition at the rotor using an azimuth-dependent Gaussian profile, an adjusted turbulence model in the near-wake region and the far-wake region and an iterative process to determine the velocity field, while considering the relation of the pressure gradient and accounting the conservation of mass. Comparison with high-fidelity simulations for a single turbine case shows a good correlation of the wake profile for both a non-misaligned and a misaligned case. Validation is performed using field lidar data, where the wake is captured within the near-wake region. The model shows a good correlation with the measurement

10 data. The performance of the modified curled wake model is further analysed within a five-turbine array, where the determined power output shows a significant improvement in comparison to other existing models. The implemented modification indicates a better representation of the near-wake region and will improve the calculation of the optimum misalignment angles for closely spaced turbines. This will aid the process of developing more accurate control-oriented wake steering models.

1 Introduction

15 Due to rapid new developments, turbines have larger rotors and thus require larger spacing between them to mitigate the effects of the wake of an upstream turbine on the power. However, due to site restrictions and minimal layout constraints turbines are being positioned with smaller relative spacing, as low as 3 rotor diameters (Nilsson et al. (2015); Hamilton (2020); Hamilton et al. (2020)), leading to a significant power loss on the downstream turbine at certain wind directions. On a wind farm level, it could lead to a power loss of up to 10% to 20%, Barthelmie et al. (2007). By steering the wake of the upstream turbines away

20 from the downstream turbines, the power losses can be reduced and an overall power gain of the wind farm can be potentially achieved. In such cases, analytical models can be used to determine the optimum yaw angle at various inflow conditions and wind directions, as they have low computational costs.

Engineering models have been developed to analytically characterise the wake deficit. The most well-known model was developed by Jensen (1983), which uses a top-hat distribution of the wake. Further advances have been made by Frandsen

25 et al. (2006), Bastankhah and Porté-Agel (2014) and Bastankhah and Porté-Agel (2016), which use a Gaussian profile of the wake deficit. Both models are based on the conservation of mass and momentum. Other approaches have been done by Larsen et al. (1996, 2008) using the Prandtl turbulent boundary equations or a simplified expression of the Navier-Stokes equations by Crespo et al. (1988). During a turbine misalignment, a counter-vortex pair is present developing the wake into a curled shape, see Howland et al. (2016). Martínez-Tossas et al. (2019) modelled the curled wake using a simplified Reynolds-averaged

30 Navier–Stokes momentum equation and solving it as a marching problem, starting from an initial condition at the rotor and moving downstream, while accounting for the counter-vortex pair and assuming no pressure gradient. By accounting for the counter-vortex pair the wake exhibits a curled wake as the turbine is intentionally misaligned. The later models give a good prediction of the wake behaviour in the far-wake as the velocity deficit is well represented by a single-Gaussian profile, but performs poorly within the near-wake region where the wake has a local minima at 75% of the span of the blade according

35 to Vermeer et al. (2003) and Aitken et al. (2014). This highlights the need to develop accurate engineering models for the near-wake region. In this work the curled wake model inside the FLORIS (FLOw Redirection and Induction in Steady State) framework is used. FLORIS is a controls-oriented framework used to test engineering wake models Annoni et al. (2018), which at the time of this study did not include a near-wake model.

Some models to estimate the velocity field within the near-wake region exists. The centreline of the wake deficit within

40 the near-wake has been modelled by Ainslie (1988) and Qian and Ishihara (2018). Magnusson (1999) derived a numerical expression of the centreline wake deficit using the momentum theory and blade element theory, along with Prandtl's approximation. Keane et al. (2016) developed a formulation based on the conservation of mass and momentum assuming a double-Gaussian profile of the wake, to resolve the entire streamwise flow field within the near-wake. This has been further improved by Schreiber et al. (2020). However, both models assume an axisymmetric wake, which does not account for the curl effects

45 during yaw misalignment and sheared inflow.

Studies investigating the near-wake region have mostly been conducted in wind tunnels using turbine models. Hu et al. (2012) investigated the flow field using PIV and found a strong correlation between the turbulent kinetic energy and the region influenced by the blade tip and root vortices. Another PIV measurement captured the coherent tip vortices and mapped the spatial variation of the mean flow and turbulent statistics within the near-wake region Zhang et al. (2012). A difference in the

50 integral length scale within the near-wake region and the far-wake region has been found in Neunaber et al. (2020)

Other measurements were conducted using a short-range WindScanner, see Hulsman et al. (2022), indicating the presence of a high energy dissipation rate at the edge of the wake within the near-wake region. Field measurements have been conducted in Dasari et al. (2019), where the wake is visualised using a super-large-scale particle image velocimetry at a utility-scale turbine. Iungo et al. (2013) used scanning Doppler lidar measurements to analyse the near-wake region of a 2MW turbine with

55 a diameter of 71 m and observed high turbulence characteristics.

The aim of this work is to implement a near-wake region ($0\,D$ to $4\,D$) within the curled wake model, to compute the flow field at various inflow conditions and misalignment angles, and to validate it against field measurements. The paper first describes the implementation of a near-wake region for a single turbine case in section 2. In section 3, the high-fidelity simulations with a single turbine are used to calibrate the model. The resulting analytically derived flow field is compared against the

60   simulation data. This is followed by validation against field data, measured using a long-range lidar. Recommendations for
     future work are highlighted in Section 4 by analysing the performance of the model within a five-turbine array indicating the
     current shortcomings of the model. The conclusion is provided in section 5.

2   Methodology

2.1   Implementing a near-wake region

65   In order to model the wake computationally efficiently, the curled wake model developed by Martínez-Tossas et al. (2019) uses
     a simplified version of the Reynolds-averaged Navier-Stokes equation for an incompressible flow, shown in Equation 1. The
     transport of momentum due to convection is included in part I of the equation. The pressure gradient is taken into account
     in part II of the equation, which is a significant factor in the near-wake region. The third part of the equation (III) represents
     the combination of turbulent and molecular diffusion. Here u is the time-averaged streamwise velocity component, v is the
70   time-averaged spanwise velocity component and w is the time-averaged vertical velocity component. Furthermore, $\overline{p}$ is the
     time-averaged pressure, ρ is the density and ν_{eff} is the effective viscosity.

$$\underbrace{u\frac{\partial u}{\partial x} + v\frac{\partial u}{\partial y} + w\frac{\partial u}{\partial z}}_{I} = \underbrace{-\frac{1}{\rho}\frac{\partial \overline{p}}{\partial x}}_{II} + \underbrace{\nu_{\text{eff}}\left(\frac{\partial^2 u}{\partial x^2} + \frac{\partial^2 u}{\partial y^2} + \frac{\partial^2 u}{\partial z^2}\right)}_{III} \tag{1}$$

The linearised version of the Reynolds-averaged Navier-Stokes equation is solved as a marching problem starting from an
initial condition at the rotor moving downstream. Within the curled wake model the assumption is made that the pressure
75   gradient can be neglected, which is only valid in the far-wake region. Furthermore, a turbulence model is used for the entire
     wake development, without considering the effects in the near-wake region. Therefore, the implementation of the near-wake
     region is done in three main steps: a more accurate representation of the initial condition at the rotor in section 2.1.1, a
     modification of the turbulence model within the near-wake region in section 2.1.2 and implementing a pressure gradient within
     the near-wake region in section 2.1.3.

2.1.1   Initial condition at the rotor

As an initial condition at the rotor at $x = 0$, the formulation for the double-Gaussian velocity deficit $U - u(r,\psi,\theta)_{x=0}$ presented
by Keane et al. (2016) is used, shown in Equation 2. This formulation is slightly modified by incorporating the blade azimuth
angle θ. This differs to Martínez-Tossas et al. (2019), where a single Gaussian profile at the rotor is applied. U represents the
free-stream streamwise velocity, $u(r,\psi,\theta)$ indicates the velocity within the wake and $C(\psi,\theta)$ is an amplitude function shown
85   in Equation 5, dependent on the yaw misalignment ψ and the blade azimuth angle. The double-Gaussian function $g(r,\sigma_{x=0})$,
     which formulates the wake shape is shown in Equation 3. Here, $\sigma_{x=0}$ indicates the width of each Gaussian profile and k is a
     calibration parameter used to adjust the wake deficit iteratively to match the thrust. The calibration method is further explained
     at the end of this section.

$$\frac{U - u(r,\psi,\theta)_{\mathrm{x=0}}}{U} = kC(\psi,\theta)\,g(r,\sigma_{\mathrm{x=0}}) \tag{2}$$

90 $$g(r,\sigma_{x=0}) = \frac{1}{2}(e^{Q-} + e^{Q+}), \qquad Q_{\pm} = -\frac{(r \pm r_0)^2}{2\sigma_{\mathrm{x=0}}^2} \tag{3}$$

The radial position of the Gaussian extrema is determined by the parameter r_0. In order to account for the change of the radial position relative to the normal cross-section y, z-plane during yaw misalignment, Equation 4 is used to determine the radius within an ellipse. The assumption is made that the position of the local extrema does not change along the blade during yaw misalignment.

95 $$r_0 = r_{0_{\psi=0°}} \frac{\cos(\psi)}{\sqrt{\cos(\psi)^2 \cos(\theta)^2 + \sin(\theta)^2}} \tag{4}$$

During a yaw misalignment, one side of the rotor ('upwind') experiences a higher angle of attack in comparison to the other ('downwind') side. This is due to the wake shedding of the 'upwind' part of the rotor according to Snel and Schepers (1995) and results in a cyclic variation of the induced velocity with regard to the azimuth angle θ. To incorporate an azimuthal dependency of the double-Gaussian function, the relation presented in Snel and Schepers (1995) to determine the streamwise

100 induced velocity is used, see Equation 5. This function is based on the expression found by Drees (1949), who included a cosinusoidal variation of blade circulation. The relationship depends on the tip speed ratio TSR, the induction factor a and the skew angle $\chi = (0.6\,a + 1)\psi$, shown in Burton et al. (2011). Here a positive yaw angle ψ is a clockwise rotation viewed from above and a positive azimuth angle is a counter-clockwise rotation viewed from the front with $0°$ at the top. The value r_{ref} is the reference position along the outer blade radius R and will be tuned to match the velocity amplitude in relation to

105 the azimuth angle seen in the high-fidelity simulation during a misalignment. The assumption is made that the variation of the streamwise induced velocity is related to the wake deficit at the rotor plane. At no yaw misalignment $C(\psi,\theta)$ is constant, but shows a cyclic change with regard to the azimuthal angle during yaw misalignment.

$$C(\psi,\theta) = a\left(1 - \frac{4}{3}\frac{r_{\mathrm{ref}}}{R}\sin\theta\tan\frac{\chi}{2}\left(1 - 1.8\left(\frac{\sin\psi}{TSR}\right)^2\right)\right) \tag{5}$$

To iteratively determine the streamwise flow field $u_{\mathrm{x=0}}$ at the rotor, the thrust from the momentum balance is equated with

110 its value from the analytical expression, shown in Equation 6. For this purpose, the streamwise momentum equation in the x-direction in integral form is used, given in Engelund (1968). A thin cylindrical control volume surrounding only the rotor is used, where a pressure increase p^+ is present at the inlet plane (right in front of the rotor) and a pressure reduction p^- is present at the outlet plane (right after the rotor). Assuming that $|p^+| = |p^-|$ the surface integration of the pressure term (second on the right) can be considered as zero. Moreover, a stationary, horizontal and inviscid flow is assumed. This means that the

115   acceleration term (first on the left), the gravity term (third on the right) and the integration of the shear stresses F_x (fourth on the

right) are negligible leading to Equation 7. Here $N_i \, \& \, N_j$ are the number of grid points in the i-direction and j-direction. It is

important to note that the flow field in front of the rotor, with a sheared profile, is considered in Equation 7 without accounting

for the induction zone. In this work, the induction zone has not been modelled. Including the induction zone would be possible,

as proposed by Branlard et al. (2020), but it would require retuning of the parameters related to the initial condition.

$$120 \quad \iiint_V \rho \frac{\partial u_{x=0}}{\partial t} dV + \iint_A \rho u_{\mathrm{x}=0}(U - u_{x=0}) dA = T_{\mathrm{flow}} - \iint_A p \, dA + \iiint_V \rho g_x dV + \iiint_V F_x dV \tag{6}$$

$$T_{\mathrm{flow}} = \rho \int_A u(r)_{x=0}(U - u(r,\psi,\theta)_{x=0}) dA \simeq \rho \sum_{i=1}^{N_i} \sum_{j=1}^{N_j} u(y_i, z_j)_{x=0}(U(y_i, z_j) - u(y_i, z_j)_{x=0}) \Delta y \Delta z \tag{7}$$

In this application, the integration of the conservation of momentum equation is solved numerically using an iterative process

within the curled wake model. During each iterative step, the thrust T_{flow} is determined using Equation 7 and compared with

the thrust T_{target} obtained from Equation 8, where c_T is the non-dimensional thrust coefficient and A the rotor area. Within

125   the FLORIS framework, the mean cubed velocity u_{eff} of the flow right in front of the turbine's rotor and within the rotor swept

area is used. During each iterative step, the calibration parameter k is increased incrementally from which a new wake deficit

and T_{flow} is computed. The process terminates until T_{flow} converges to T_{target}.

$$T(\psi)_{\mathrm{target}} = 0.5\rho c_T \cos(\psi) A u_{\mathrm{eff}}^2 \tag{8}$$

2.1.2 Turbulence model

130   Besides the incorporation of the initial starting condition at the rotor, the turbulence model within the curled wake model is

modified. Multiple approaches have been applied to estimate ν_{eff}. Martínez-Tossas et al. (2019) used the mixing length model

$\ell_m = \kappa z/(1 + \kappa z/\lambda)$ to compute $\nu_{\mathrm{eff}} = \ell_m^2 |du/dz|$ with the von Karman constant κ, the velocity gradient du/dz and the

$\lambda = 15\,m$ which corresponds to the value reached by ℓ_m in the free atmosphere. Further work done by Bay et al. (2020) added

the decay of the vortices shed by the yaw misaligned turbine as they move downstream, which was not included in Martínez-

135   Tossas et al. (2019). Bay et al. (2020) proposed a relation to determine the added turbulence $I_+ = 0.73a^{0.8}I_0^{0.1}(x/D)^{-0.275}$

using the axial induction a and the turbulence upfront of the turbine I_0 in the Reynolds-averaged Navier-Stokes equation,

resulting in Equation 9. Here parameter ξ is an adjustable dimensionless tuning parameter used to modify the decay of the

wake. The model is based on the relation from Crespo et al. (1996), where the empirical values are tuned based on previous

FLORIS studies. However, the model used from Crespo et al. (1996) is only applicable for the far-wake and a tuning by Bay

140   et al. (2020) was needed, as it is used for both regions.

$$u\frac{\partial u}{\partial x} + v\frac{\partial u}{\partial y} + w\frac{\partial u}{\partial z} = -\frac{1}{\rho}\frac{\partial \overline{p}}{\partial x} + \xi I_+ \nu_{\mathrm{eff}}\left(\frac{\partial^2 u}{\partial x^2} + \frac{\partial^2 u}{\partial y^2} + \frac{\partial^2 u}{\partial z^2}\right) \tag{9}$$

For the near-wake region Crespo et al. (1996) proposes the relation $I_+ = 0.725a$ to compute the added turbulence in the near-wake region. For the added turbulence in the far-wake region Crespo et al. (1996) derived the equation $I_+ = 0.73a^{0.8325}I_0^{-0.0325}(x/D)^{-0.32}$. Similar to Bay et al. (2020) these two equations are modified within the modified curled wake model to adjust the wake decay within the wake resulting in $I_+ = 0.4a$ and $I_+ = 0.8a^{0.8325}I_0^{-0.0325}(x/D)^{-0.1}$. Furthermore, a definition is required to determine the starting point x_0 at which the pressure gradient is considered to be negligible and when the far-wake region starts. This information is necessary as the turbulence model changes in the far-wake region. Not applying a threshold results in the use of only the turbulence model intended for the near-wake region for the entire wake. For this application, Equation 10, derived using the analogy to determine the length of a potential core for a round jet, shown in Bastankhah and Porté-Agel (2016), is used. The values α_{NW} and β_{NW} are tuneable parameters, which can be tuned to estimate the length of the near-wake region. Bastankhah and Porté-Agel (2016) reported a value of $\beta_{\mathrm{NW}} = 0.077$, based on the studies of jet flows, and a value of $\alpha_{\mathrm{NW}} = 0.58$ that provided acceptable predictions for $x_0 \approx 4D$ with their wind tunnel measurement data. In this study the parameter α_{NW} is adjusted to 1.16 to achieve acceptable predictions for $x_0 = 2.25\,D$ with the numerical simulations, which corresponds to the findings of Sanderse (2009) indicating a transition of the near-wake region to the far-wake region at $2\,D$.

$$\frac{x_0}{D} = \frac{\cos\psi(1 + \sqrt{1 - c_T})}{\sqrt{2}(4\alpha_{\mathrm{NW}}I_0 + 2\beta_{\mathrm{NW}}(1 - \sqrt{1 - c_T}))} \tag{10}$$

2.1.3 Pressure gradient

The final step to introduce a near-wake region within the curled wake model is to compute the pressure gradient at each marching step within the near-wake region. This is done using an iterative process, shown in Figure 1. As the curled wake model uses a forward-time, centred-space method, the applied iteration process is utilised at each marching step. The equation for the marching problem, shown in Equation 11 is derived using a first-order forward discretisation for the streamwise derivative and second-order finite differencing for the spanwise derivatives Martínez-Tossas et al. (2019). Here u', v' and w' are the perturbation velocities defined as $u = U + u'$, $v = V + v'$ and $w = W + w'$ respectively, with U, V, W being the base flow and u', v', w' describing the deficit. The term ∇^2 is the wall-normal and spanwise components of the Laplacian operator.

$$u'_{i,j,k} = u'_{i-1,j,k} - \frac{\Delta x}{(U + u')_{i-1,j,k}} \left(W_{i-1,j,k} \frac{(U + u')_{i-1,j,k+1} - (U + u)_{i-1,j,k-1}}{\Delta z} \right.$$
$$\left. + V_{i-1,j,k} \frac{u'_{i-1,j+1,k} - u'_{i-1,j-1,k}}{\Delta y} - \xi I_+ \nu_{\mathrm{eff}} \nabla^2 u'_{i-1,j,k} + \frac{1}{\rho}\frac{\Delta p}{\Delta x} \right) \tag{11}$$

Within each iteration step, the pressure gradient is determined using Bernoulli's principle: $\Delta p / \Delta x = 1/2\rho((U + u')^2_{i,j,k} - (U + u')^2_{i-1,j,k})$. In the ideal case, the iteration process is aborted when the divergence ∇u, obtained with Equation 12, reaches zero, indicating conservation of mass. However, due to the imposed vortices at the rotor within the curled wake model and the assumptions used, the divergence will never reach exactly zero. As the analytical model is not able to capture all physical phenomena properly, a weighting function (see Equation 13) is introduced to enforce that the divergence is converging better
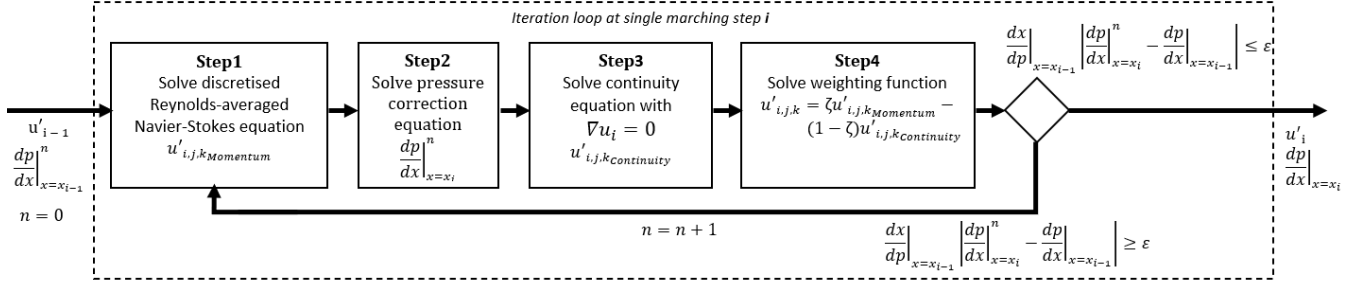
Figure 1. Iterative process to obtain the pressure gradient at a marching step i, using the pressure gradient $\frac{dp}{dx_{i-1}}$ as a starting point. The curled wake is solved using a forward-time centred-space method, where the flow field $u(y,z)_{i-1}$ is used to compute $u(y,z)_i$. The iteration is aborted when the change in the pressure gradient is below $\varepsilon = 10^{-6}$

to zero, where the new velocity field during each iteration-loop is calculated based on the momentum equation (Equation 11) and the continuity equation (Equation 12) with $\nabla u = 0$.

$$\nabla u = \frac{(U + u')_{i,j,k} - (U + u')_{i-1,j,k}}{\Delta x} + \frac{(V + v')_{i,j,k} - (V + v')_{i,j-1,k}}{\Delta y} + \frac{(W + w')_{i,j,k} - (W + w')_{i,j,k-1}}{\Delta z} \quad (12)$$

Here, ζ is a weighting parameter and a value of 0.85 is used for this analysis, after experimenting with different values, and
175 proved to enforce the divergence the closest to zero. This leads to a calculated flow field that better represents the conservation of mass (although not fully). To abort each iteration, a threshold ε related to the difference of the pressure gradient during each iteration-loop is used. The process is aborted when the change in the pressure gradient is below $\varepsilon = 10^{-6}$. It is observed that ∇u is close to zero at the end of each iteration process except at the edge of the rotor where the vortices are imposed. The pressure gradient is set to zero within the far-wake region, and the start of the region is obtained using Equation 10.

180 $\quad u'_{i,j,k} = \zeta u'_{i,j,k_{\text{Momentum}}} + (1 - \zeta)u'_{i,j,k_{\text{Conservation}}}$ $\quad (13)$

To summarise, the adaption to the curled wake model introduces the following tuneable parameters to model the near-wake region which have been adjusted using the high-fidelity simulations with a single turbine: 1) radial position of the Gaussian extrema r_0 2) radial position used as a reference to indicate the azimuthal change of the streamwise velocity component at the rotor r_{ref} 3) width of each Gaussian profile $\sigma_{x=0}$ 4) weighting parameter to obtain a better representation of the conservation
185 of mass ζ 5) α_{NW} and β_{NW} to determine the near-wake length. Lastly, the added turbulence I_+ within the near-wake region and the far-wale region are modified.
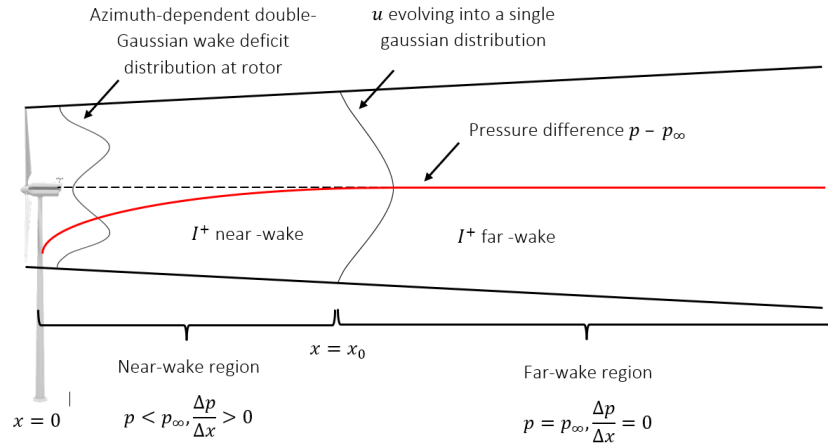
Figure 2. Overview of the main modifications to implement a near-wake region in the curled wake model. At the rotor, an azimuth-dependent double-Gaussian wake distribution is used to satisfy the conservation of momentum. Furthermore, a separate turbulence model is used in the near-wake region and in the far-wake region. The pressure gradient is determined using an iterative process.

2.2 High-fidelity numerical simulation

To tune the modified curled wake model, a high-fidelity numerical simulation is performed using a coupling between the PArallelised Large eddy simulation Model (PALM) (revision model 3193), see Maronga et al. (2015), and the aeroelastic tool FAST v8 developed by Jonkman et al. (2005). As the wake deficit within the near-wake region is mainly determined by the lift distribution on the blade, PALM is used to simulate a highly detailed representation of the flow field in the near-wake region. Here the actuator sector method ASM is used by Krüger et al. (2022), where the blade movement is described as a segment of a circle within PALM. The aerodynamic forces based on the local flow on each separate blade segment are computed within FAST and then applied to the flow within PALM. As field lidar measurements within the near-wake are existing (see subsection 2.3), the numerical simulation is performed using an aeroelastic model of the eno126 3.5MW turbine. A turbine-specific BLADED model is provided by eno energy, which is then converted into FAST. The eigenfrequencies of the tower and blades obtained in FAST were calibrated using load data from field measurements. Here, the coupling approach developed by Krüger et al. (2022) is used, which is an improvement of the work described in Bromm et al. (2017).

PALM uses the non-hydrostatic incompressible Boussinesq approximation of the Navier-Stokes equations and the Monin-Obukhov Similarity Theory, to exchange information between the surface and the lowest grid cell. The simulation is executed using a grid size of $2555\,\mathrm{m}\,(\approx 20\,D)$ x $800\,\mathrm{m}\,(\approx 6\,D)$ x $10235\,\mathrm{m}\,(\approx 81\,D)$ with a grid spacing $\Delta = 5\,\mathrm{m}$ and a turbulent recycling distance of $5500\,\mathrm{m}$, where the instantaneous flow field of the precursor simulation is introduced into the main simulation. A surface temperature of $283.15\,\mathrm{K}$ is used with a temperature gradient of $8\,\mathrm{K}/100\,\mathrm{m}$ starting at $500\,\mathrm{m}$ up to $600\,\mathrm{m}$, where a temperature gradient of $1\,\mathrm{K}/100\,\mathrm{m}$ starts. A constant geostrophic wind at the surface is used with $u_g = 9.49\,\mathrm{m/s}$ and $v_g = -3.57\,\mathrm{m/s}$. The following boundary conditions were used: 'Neumann' at the surface, 'radiation' at the outlet and

'Dirichlet' at the inlet. Furthermore, at the inlet a turbulence recycle method is used and a roughness length of 0.1 m. The total simulation time is 5400 s of which the first 1800 s were omitted to account for the transient period. The flow is extracted at $x = [-3.7\,D, 1\,D, 2\,D, 3\,D, 5\,D, 7\,D, 10\,D]$ with $0\,D$ being the turbine location. The inflow parameters are determined at $-3.7\,D$ resulting to a vertical shear of $\alpha = 0.27$, a wind veer along the rotor swept area $\theta_{\text{veer}} = 3.74°$, a hub height wind speed

210 $U_{\text{hub}} = 7.83\,\text{m/s}$ and $\text{TI} = 6.80\%$. The PALM-FAST coupled simulations are performed for two yaw misalignment cases with a single turbine and three yaw misalignment cases with 5 turbines in a row with a spacing of $2.7\,D$, an overview is shown in Table 1. The later cases are used to evaluate the performance of the modified curled wake model in a turbine array.

	ψ_{WT1}	ψ_{WT2}	ψ_{WT3}	ψ_{WT4}	ψ_{WT5}
Case 1	$0°$	-	-	-	-
Case 2	$30°$	-	-	-	-
Case 3	$0°$	$0°$	$0°$	$0°$	$0°$
Case 4	$30°$	$0°$	$0°$	$0°$	$0°$
Case 5	$20°$	$15°$	$10°$	$5°$	$0°$

Table 1. Yaw misalignment settings of the five simulation cases with a single turbine and a turbine array respectively.

2.3 Field lidar measurements within the near-wake region

The field data were obtained from a measurement campaign conducted in July 2021 at a wind farm with two 3.5 MW wind

215 turbines, with a diameter D of 126 m, in Kirch Mulsow in cooperation with eno energy systems GmbH. At the site, a ground-based lidar, a met mast and yaw sensors are installed. Here only the wake measurement of turbine WT2 with a hub height of 137 m is analysed. With the ground-based lidar WindCube 200s positioned $4.1\,D$ away from WT2 and $2.6\,D$ from the met mast, the wake at $0.5\,D$ and at $1\,D$ is reconstructed using measurements from multiple plan position indicator (ppi) scans. The measurements were then interpolated onto a 12×13 grid with a spatial grid size of 20 m ($0.16\,D$), where $z \in$

220 $[46.48\,m, 66.48\,m, ..., 266.48\,m]$ and $y \in [-120\,m, -100\,m, ..., 120\,m]$. Each scan is preformed with a duration of $t_{scan} \approx 18\,s$, a scanning area within the azimuth angle $\theta_{\text{Lidar}} \in [2.65°, 35.45°]$, where $0°$ is north rotating clockwise, and an elevation angle at $[5.92°, 8.25°, 10.57°, 12.90°, 15.08°, 17.55°, 19.88°, 22.21°, 24.53°, 26.86°]$ sequentially. The two turbines have a hub height h of 117 m (WT1) and 137 m (WT2) with a distance of $2.7D$, shown in Figure 3. The measurements were conducted, when WT1 was not operational, with an incoming wind direction around $48°$. This is to ensure that the measurements of the near-

225 wake are not disturbed due to the induction zone of WT1. Using the line-of-sight velocity, the horizontal component is extracted with Equation 14 using the elevation angle γ and the relative azimuth angle between the laser beam and the incoming wind direction $\theta_{\text{Lidar}} - \theta_{\text{Wind}}$ of each measurement point.

$$u = \frac{V_{\text{LOS}}}{\cos(\gamma)\cos(\theta_{\text{Lidar}} - \theta_{\text{Wind}})} - \frac{v\sin(\theta_{\text{Lidar}} - \theta_{\text{Wind}})\cos(\gamma)}{\cos(\gamma)\cos(\theta_{\text{Lidar}} - \theta_{\text{Wind}})} - \frac{w\sin(\gamma)}{\cos(\gamma)\cos(\theta_{\text{Lidar}} - \theta_{\text{Wind}})} \approx \frac{V_{LOS}}{\cos(\gamma)\cos(\theta_{\text{Lidar}} - \theta_{\text{Wind}})}$$

$$(14)$$
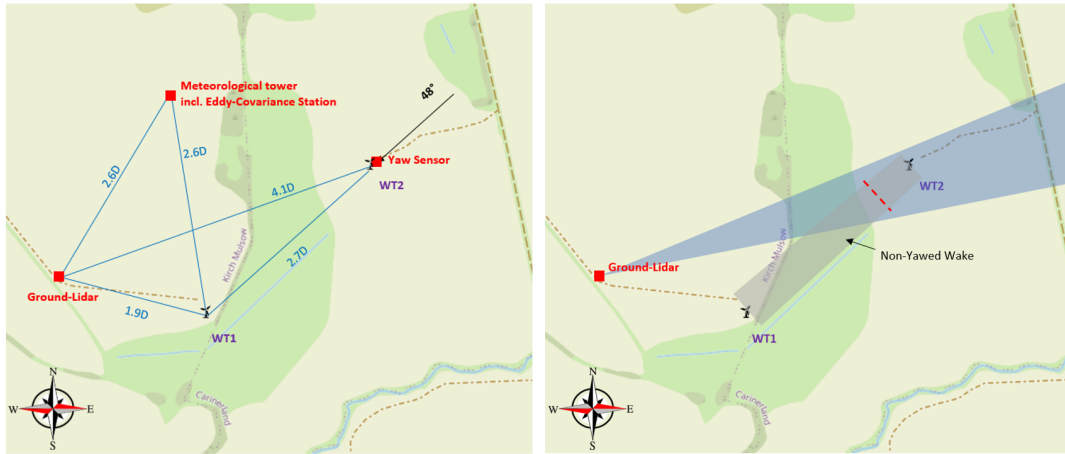
Figure 3. Left: Layout of the experimental field campaign. The position of both turbines, the met mast and the ground-based lidar are shown. The upstream turbine (WT1) and the downstream turbine (WT2) are equipped with a GPS-based yaw sensor. **Right:** Illustration of the ground-based lidar scan measuring in the near-wake of WT2. Map data from © OpenStreetMap

The assumption is made that the lateral and vertical velocity components are negligible, $v \approx 0$ and $w \approx 0$, respectively. How-
230 ever, within the near-wake region a large lateral and vertical velocity component is expected, which influences the calculation for the streamwise velocity component. A dynamic filtering process is applied based on the approach presented in Beck and Kühn (2017), using a kernel density function to filter out the outliers within each scan.

A met mast (MM) equipped with a cup anemometer and a wind vane at 54 m and 112 m is used to measure the inflow condition at 50 Hz. An additional sensor to capture the temperature and the pressure is installed at 110 m. Moreover, the
235 atmospheric stratification is captured using three Eddy-Covariance Stations at a height of 2 m, 6 m and 54 m every 30 min. SCADA data for WT2, including signals such as turbine power, turbine heading and turbine status, are stored at 10 Hz.

3 Results and discussion of the modified curled wake model

This section presents the results for a single turbine case obtained with the curled wake model incorporated with a near-wake region, referred to as the 'modified curled wake model'. At first, numerical results related to the implementation of the near-
240 wake region are provided. Furthermore, a comparison to other wake models and high-fidelity simulations is provided using a single turbine. In the following, we refer to the models presented by Bastankhah and Porté-Agel (2016) and by Martínez-Tossas et al. (2019) as the 'Gaussian wake model' and the 'original curled wake model', respectively. The analytical calculation is performed using the inflow conditions obtained from the high-fidelity simulation. Lastly, a validation is performed using field measurements. As described in Section 2 the modified curled wake model is calibrated using the single turbine case which
245 resulted in the following parameters: $r_0 = 0.68R$, $r_{\mathrm{ref}} = 0.2R$, $\sigma_{x=0} = 0.32R$, $\zeta = 0.8$, $\alpha_{\mathrm{NW}} = 1.16$ and $\beta_{\mathrm{NW}} = 0.77$. The resulting outcome of the modified curled wake model is depicted.

3.1 Numerical implementation of the near-wake region

As described in section 2.1, the first step to implement a near-wake region is the definition of the initial condition at the rotor. This is seen in Figure 4, where the initial condition at $0\,D$ of the original curled wake model (Figure 4a and 4c) is compared to the initial condition of the modified curled wake model (Figure 4b and 4d) at $\psi = 0°$ and $\psi = 30°$ viewing at the streamwise velocity component (u). Due to the presence of shear in both cases, a variation of u is noticeable within the wake over the height. In the original curled wake model, the initial profile is set as a uniform distribution computed with $u' = -2aU_{\mathrm{hub}}$, which is smoothed with a Gaussian filter to avoid numerical instabilities. In contrast to the original curled wake model, the double-Gaussian profile is visible in the modified curled wake model. At $\psi = 0°$ no azimuthal variation is present due to yaw, but it is visible in Figure 4d with $\psi = 30°$. There, u at hub height is lower at $\approx 0.3y/D$ in comparison to $\approx -0.3y/D$ and the highest wake deficit is shifted to $\approx 0.1y/D$, as a result of the interaction with the boundary layer. In both cases, the wake

(a) Original curled wake model, $\psi = 0°$

(b) Modified curled wake model, $\psi = 0°$

(c) Original curled wake model, $\psi = 30°$

(d) Modified curled wake model, $\psi = 30°$
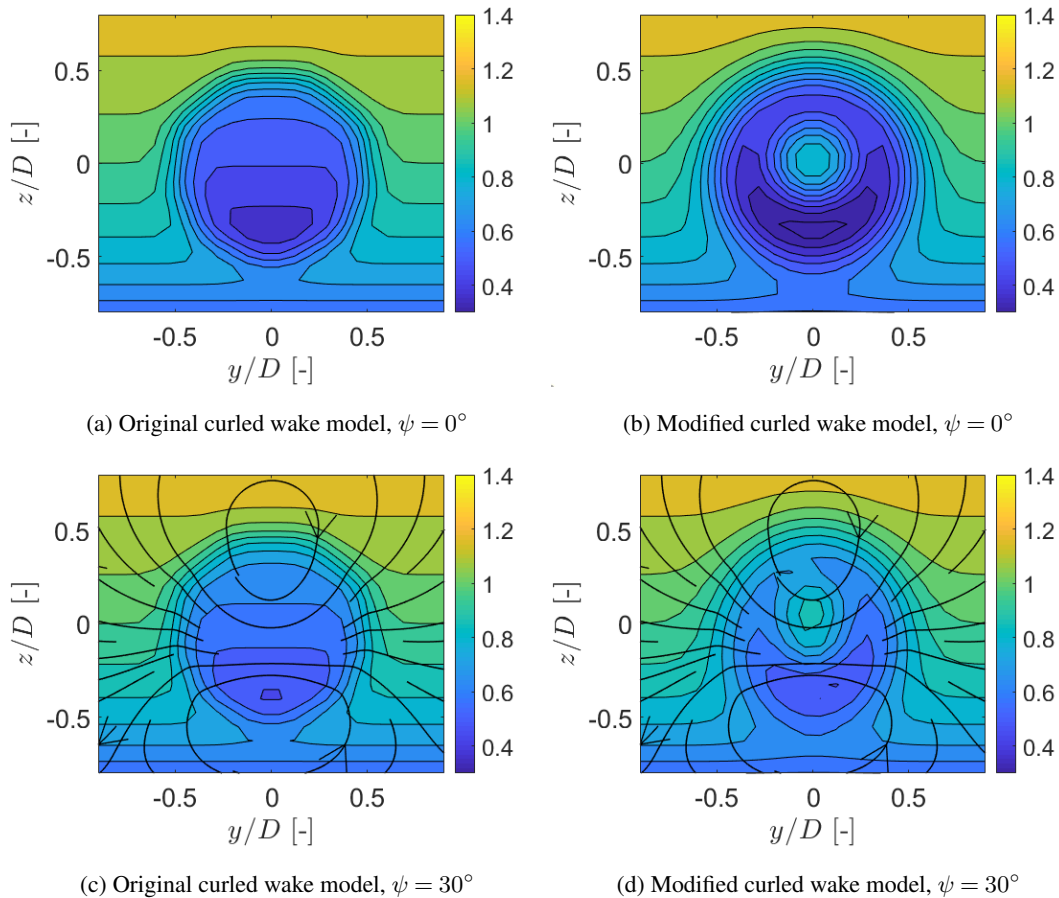
Figure 4. Initial condition at the rotor u/U_{hub} within the original curled wake model and the modified curled wake model for $\psi = 0°$ and $\psi = 30°$ looking downstream. The streamlines show the spanwise velocity vector.

deficit reduces due to the reduction of the thrust component during yaw misalignment. Since the figures represent the wake deficit at $0\,D$, no wake deflection is observed. Moreover, as formulated in Equation 4, the wake in Figure 4d represents an elliptical shape. Through the improved initial condition in the modified curled wake model, a better representation is achieved

260 as the wake propagates downstream, shown in Section 3.2. The imposed vortices at the rotor within the curled wake model are identical for the original curled wake model and the modified curled wake model, visualised using streamlines in Figure 4.

The second step to integrate a near-wake region within the curled wake model is to account for the pressure gradient. This has been done using an iterative process at each spatial marching step, as described in Section 2. The pressure field computed with the modified curled wake model is shown in Figure 5a at $\psi = 0°$ and at $0\,D$, where a positive pressure gradient

265 is computed between $0.2 < r/D < 0.5$ over the blade radius. Due to the incoming wind, a pressure difference is generated between a so-called 'suction' side and a 'pressure' side on the surface of the blade according to Madsen et al. (2019). The
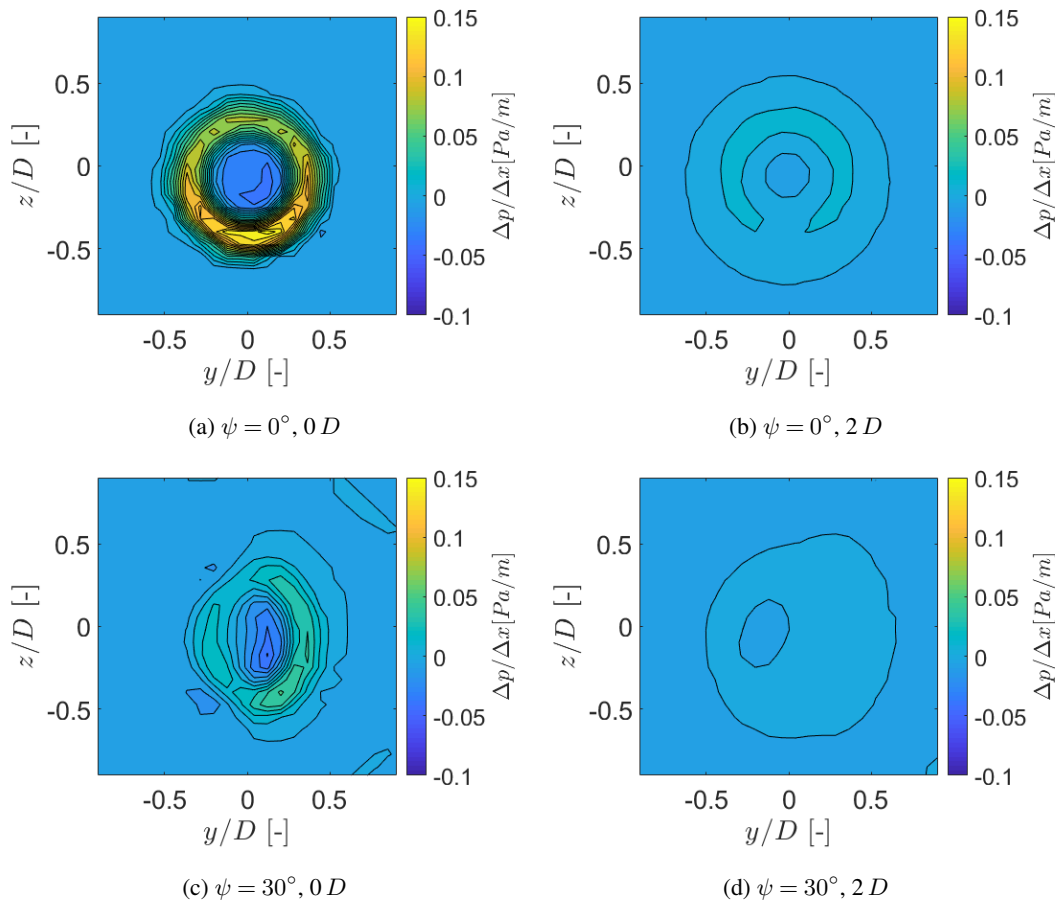
Figure 5. Contour plot of the pressure gradient over a vertical cross-section with $\psi = 0°$ and $\psi = 30°$ at $0\,D$ and $2\,D$ computed using the modified curled wake model

difference in the pressure distribution over the blade airfoil results in the lift and drag force. Ronsten (1992) has shown that the pressure distribution changes depending on the radial position, which inherently leads to a radial change of the lift and thrust components. Ronsten (1992) performed static pressure measurement on a rotating model turbine blade inside a wind tunnel and observed a radial decrease of the pressure to the minimum at $r/R = 0.85$ after which it increased until the rotor tip. A similar effect is also simulated in Madsen et al. (2019) and indicated that the radial change of the pressure distribution is blade specific. As the blade rotates, the interaction between the 'pressure' side and the 'suction' side generates vortex structures and hence influences the velocity distribution within the near-wake. Furthermore, it is expected that the 'suction' side influences the pressure field within the near-wake region and that the pressure recovers further downstream. The radial variation of the pressure gradient field seen in Figure 5a is expected, as the pressure distribution over the blade changes along the radius. The negative pressure gradient region between $0 < r/D < 0.2$ directly results from the initial condition defined at the rotor. Due to the double-Gaussian profile at the rotor, the velocity at the turbine centre $r/D \approx 0$ is lower in comparison to the wake velocity at $r/D \approx 0.4$. As the wake evolves into a single Gaussian shape the velocity deficit at the centre line needs to increase within the near-wake region, after which it decays in the far-wake region and with it a velocity increase. When applying Bernoulli's principle at the wake centre in the near-wake region, a negative pressure gradient is obtained. Further investigation is required to determine if the negative pressure gradient region is visible in experimental data or high-fidelity simulations, as it could be a direct result of the blade root profile, hub and nacelle geometry. At $\psi = 30°$, the pressure gradient field is no longer axisymmetric, due to the azimuthal dependency of the initial condition at the rotor (Equation 5) and the change of the radial position of the Gaussian extremum (Equation 4). This results in a larger positive pressure gradient at $y/D > 0$ and an elliptical shape of the negative pressure gradient region at the centre. Figure 5b and Figure 5c visualise the pressure gradient field at a
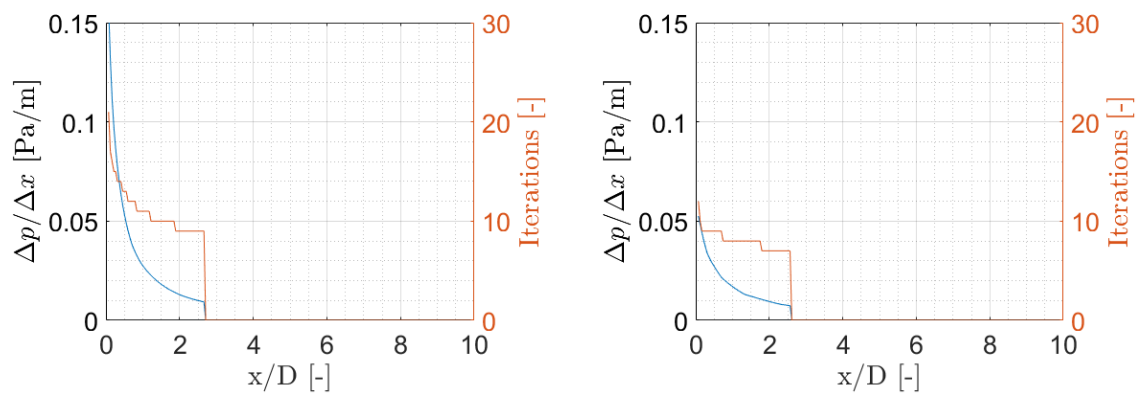
Figure 6. Development of the maximum pressure gradient within the wake and the number of calculations to reach a convergence within the modified curled wake model for $\psi = 0°$ (**Left**) and $\psi = 30°$ (**Right**). The calculation is aborted using the near-wake length formulation by Bastankhah and Porté-Agel (2016) indicating the start of the far-wake region with $\frac{\Delta p}{\Delta x} = 0$. At this point, the pressure gradient within the near-wake region has not fully converged to zero yet.

downstream distance of $2\,D$ for both yaw cases, where the magnitude of the gradient has decreased as the near-wake region transitions to the far-wake region.

The development of the pressure gradient downstream is depicted in Figure 6 for $\psi = 0°$ and $\psi = 30°$, including the number of iterations needed to obtain a convergence during the iteration process at each marching step. As described in Section 2 the

290 iterations are aborted when the pressure gradient change is below $\varepsilon < 10^{-6}$. As described in section 2.1.3, the near-wake length is determined based on Bastankhah and Porté-Agel (2016) and $\Delta p/\Delta x$ is set to zero at the start of the far-wake region. A higher pressure gradient is observed at $0\,D$ for the case with no yaw misalignment in comparison to $\psi = 30°$, due to the reduction of the thrust component during yaw. This results in a reduction of the needed iteration steps to reach convergence.

3.2 Comparison with high-fidelity simulations

295 The analytically computed wake decay of the modified curled wake model is compared against the numerical simulations with and without a misalignment for a single turbine case. As indicated in the previous section these simulation cases are used to
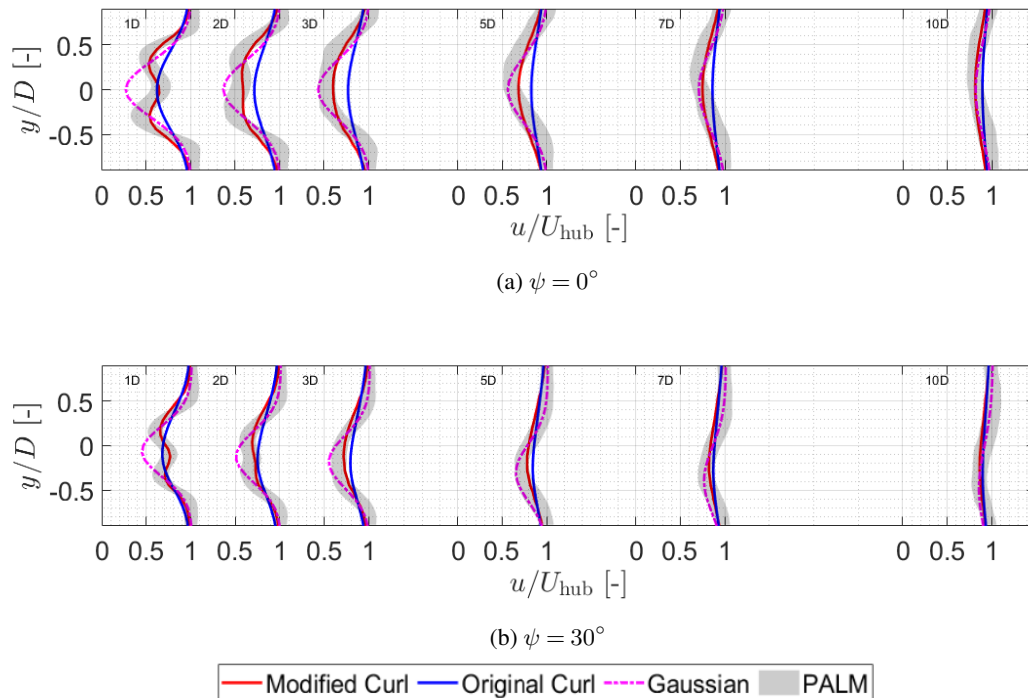
Figure 7. Comparison of the horizontal wake profile at hub height between the original curled wake model (**blue**), the modified curled wake model (**red**), the Gaussian wake model (**purple**) and the high-fidelity simulations (**grey**) within PALM using the horizontal wake deficit u/U_{hub} at hub height at $1\,D$, $2\,D$, $3\,D$, $5\,D$, $7\,D$ and $10\,D$ with $\psi = 0°$ (**Top**) and $\psi = 30°$ (**Bottom**). The shaded grey area represent $u/U_{\mathrm{hub}} \pm \sigma_{\mathrm{u}/U_{\mathrm{hub}}}$ from the high-fidelity simulations.

calibrate the near-wake region. For the non-misaligned case, the shortcomings of the original curled wake model are clearly visible as it overpredicts the velocity within the near-wake region until it converges towards the other models in the very far wake. This is depicted in Figure 7, where the normalised wake deficit u/U_{hub} at hub height at $1\,D$, $2\,D$, $3\,D$, $5\,D$, $7\,D$ and

300    $10\,D$ computed with the original curled wake model (**blue**), the modified curled wake model (**red**), the Gaussian wake model (**purple**) and the high-fidelity simulations (**grey**) is illustrated. As a result of the implementation of a uniform initial wake deficit at the rotor, the wake follows a Gaussian profile which recovers further downstream. The modified curled wake model leads to a more accurate estimation of the velocity deficit within the near-wake region as it corresponds very well with the high-fidelity simulations. The model follows a double-Gaussian profile at $1\,D$, which decays into a single Gaussian profile in

305   the far-wake region. The Gaussian wake model also does not correspond to the high-fidelity simulations until $3\,D$.

At a yaw misalignment of $\psi = 30°$ (Figure 7b), the double-Gaussian distribution within the modified curled wake model is no longer axisymmetric, due to the azimuthal dependency of the initial condition at the rotor. As described in Section 3.1, a higher wake deficit at $\approx 0.3y/D$ is observed in comparison to $\approx -0.3y/D$ at hub height. Here, the results of the modified curled wake model resemble high-fidelity simulations as the wake develops downstream. Furthermore, the position of the

310   Gaussian extremum obtained from the modified curled wake model corresponds well with the high-fidelity simulations as it
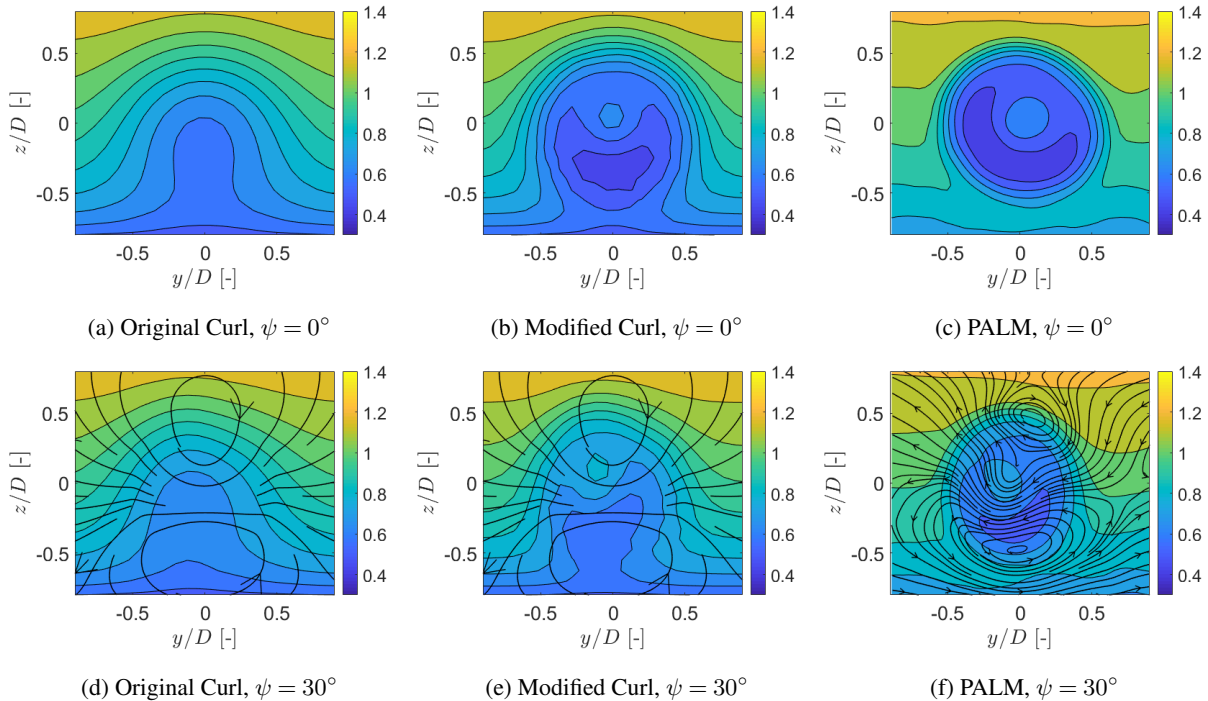
Figure 8. Comparison of the vertical cross-section between the original curled wake model, the modified curled wake model and the high-fidelity simulations within PALM using u/U_{hub} in the vertical plane at $1\,D$. The streamlines show the spanwise velocity vector.

decays downstream for $\psi = 0°$ and $\psi = 30°$. This is not the case for the original curled wake model and the Gaussian wake model in the near-wake region.

The streamwise velocity contours u/U_{hub} at $1\,D$ are computed using the original curled wake model, the modified curled wake model and the high-fidelity simulations for $\psi = 0°$ and $\psi = 30°$, see Figure 8. The streamlines of the transverse flow are

315   only visualised for the case with a yaw misalignment. For the non-misaligned case, it can be seen (besides the difference due to the initial condition) that the wake decays faster for the original curled wake model in comparison to the modified curled wake model. This becomes clearer when looking at the initial wake deficit at the rotor (Figure 4). Furthermore, Figure 8b depicts a steeper wake edge for the modified curled wake model in comparison to the original curled wake model (Figure 8a). This is related to the applied turbulence model, where a specific model is implemented in the modified curled wake model for

320   the near-wake region based on Crespo et al. (1996). Similar behaviour is noticeable for the misaligned case. The streamlines illustrating the spanwise velocity vector are identical for the original curled wake model and the modified curled wake model. Within the curled wake model described in Martínez-Tossas et al. (2019), the rotational velocity caused by yawing and the rotational velocity caused by the blade rotation are applied by the method of superposition on the base flow. This means that the spanwise velocity is pre-computed for the entire domain and that only the streamwise velocity is solved. Hence modifying

325   the computation of the streamwise velocity component (done in the modified curled wake model) does not affect the spanwise

(a) Original Curl, $\psi = 0°$ (b) Modified Curl, $\psi = 0°$ (c) PALM, $\psi = 0°$

(d) Original Curl, $\psi = 30°$ (e) Modified Curl, $\psi = 30°$ (f) PALM, $\psi = 30°$
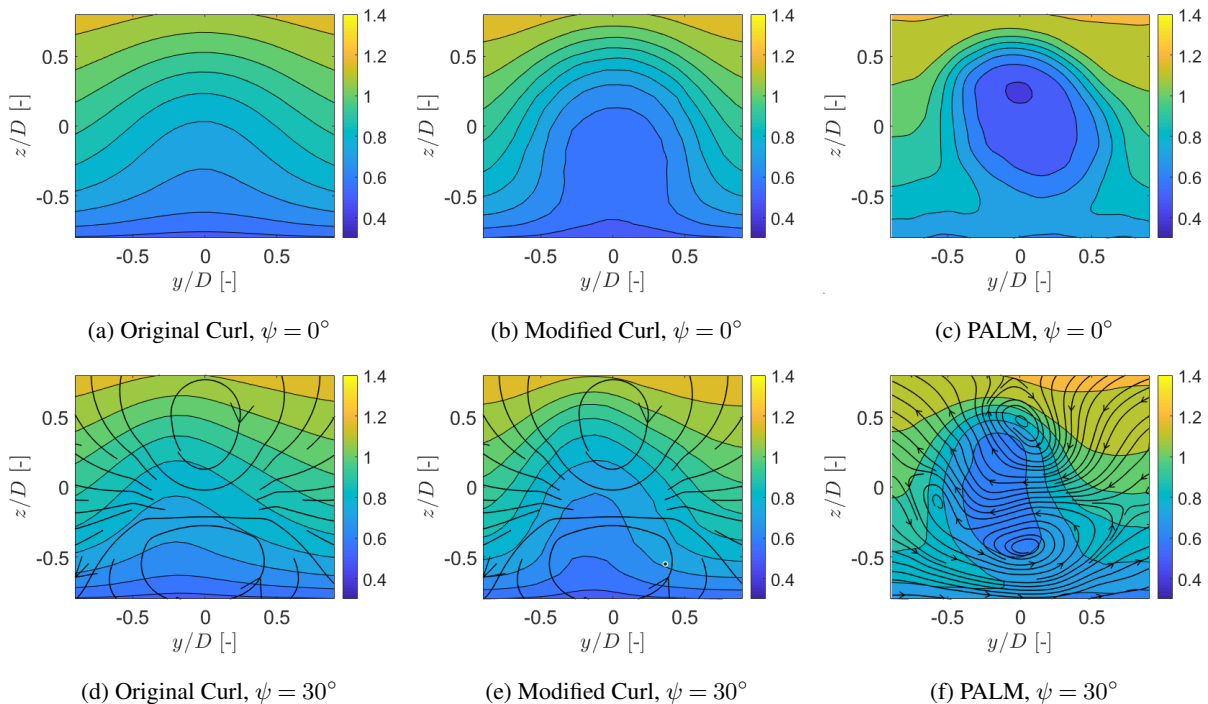
Figure 9. Comparison of the vertical cross-section between the original curled wake model, the modified curled wake model and the high-fidelity simulations within PALM using u/U_{hub} at $3\,D$. The streamlines show the spanwise velocity vector.

velocity. As a result of the presence of the applied vortices, the core of the near-wake (the region with a higher velocity deficit at the centre) is pushed to the left in Figure 8e. This matches the results from the high-fidelity simulations in Figure 8f, where a similar magnitude of the displacement of the core is observed.

At $3\,D$ (Figure 9) the wake has decayed further and the core, visible before within the near-wake region, is fully decayed for the non-misaligned cases (Figure 9c) and the misaligned cases (Figure 9f) observed within the high-fidelity simulations. Similarly, the modified curled wake model (Figure 9b and 9e) also does not follow a double-Gaussian profile at this point. Based on the contour-lines visualised in Figure 9b, the edge of the wake decays faster in comparison to the high-fidelity simulation (Figure 9c). This could be due to the product of the applied turbulence model from Crespo et al. (1996) and the term ∇^2 in Equation 11, accounting for the velocity gradient, which determines the wake decay. This shows that further development is needed to improve the turbulence model and its relation with the velocity gradient. The wake deficit at the centre (see Figure 7a-7b) matches well with the high-fidelity simulations.

3.3 Validation against field data

After analysing the performance of the modified curled wake model for a single turbine case in comparison to other models, the model is validated using field data. As described in Section 2, the wake deficit within the near-wake region at $0.5\,D$ and at $1\,D$ is measured using a ground-based lidar with multiple scanning planes. The measurement period was $\approx 43\,\text{min}$ resulting in 142 individual scans and 14 complete scans of the wake, during which the averaged inflow parameters of $U_{\text{hub}} = 5.6\,\text{m/s}$, $\text{TI}_{\text{hub}} = 10.8\%$, $\alpha = 0.21$, $\theta_{\text{WD}} = 49.0°$ and $\theta_{\text{Veer}} = 0.0°$ is measured using the met mast. During this time period, a stability parameter of $z/L = -0.01$ is measured corresponding to a neutral atmospheric stratification. The average wind speed, turbulence intensity and shear were used as input to the modified curled wake model to compute the flow field within the near-wake region. Through the use of the GPS-sensors, an average yaw misalignment of $0.9°$ was present during the period of interest where the turbine heading changed three times to follow the wind direction. Due to the procedure of performing multiple lidar scans, the duration to capture the entire wake is $180\,\text{s}$. This leads to a different inflow condition and turbine heading at different measurement points within the wake. To account for the change of the turbine heading, as it follows the fluctuations of the wind direction around $48°$, the measurement points were reconstructed on a reference frame attached to the turbine nacelle (NFoR). This means that the reference frame is rotating with the nacelle during yaw manoeuvres as it follows the wind direction changes, see Conti et al. (2021). This is done to perform a direct comparison to the results from the original curled wake model, as no wind direction variability is present during the analytical calculation.

Figure 10 presents the results from the reconstructed wake within the near-wake region in comparison to the modified curled wake model using the tuned parameters determined with high-fidelity simulations, shown in Section 2. The field data indicates a clear presence of a double-Gaussian profile at $0.5\,D$ and at $1\,D$. Similar behaviour is also observed in Dasari et al. (2019), where the wake is visualised using a super-large-scale particle image velocimetry at a utility-scale turbine. Iungo et al. (2013) also measured the near-wake region using a lidar, but did not observe a double-Gaussian profile. The wake deficit shown in Figure 10a, points to a wake position of $0.15\,D$ at $0.5\,D$ whereas the wake position is at $0\,D$ at a downstream distance of $1\,D$. Since the measurements at $0.5\,D$ and $1\,D$ were performed simultaneously and not sequentially, similar inflow conditions

(a) Vertical plane at $0.5\,D$ (b) Comparison using u/U_{hub} at hub height

(c) Vertical plane at $1\,D$ (d) Comparison using u/U_{hub} at hub height
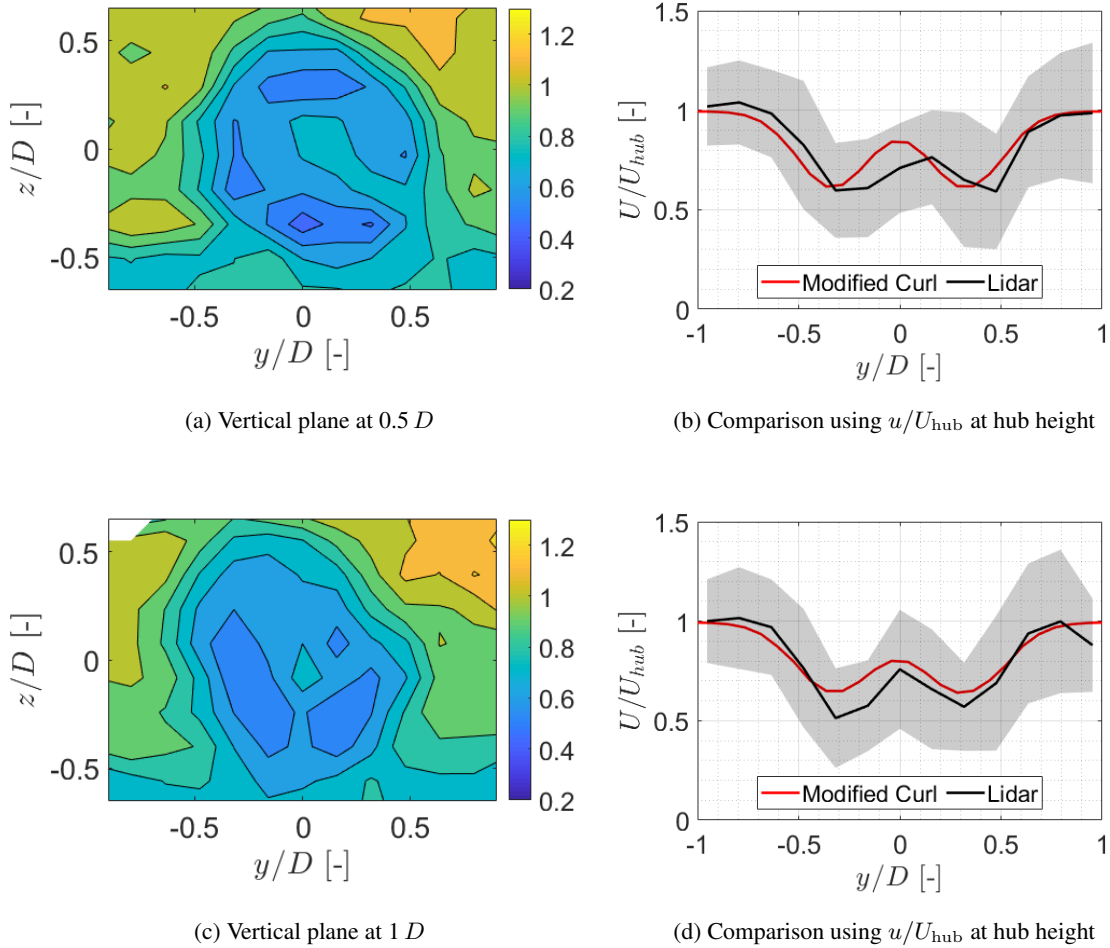
Figure 10. Vertical scan at $0.5\,D$ and $1\,D$ captured by the ground-based lidar. A comparison between field measurements and the modified curled wake model is shown using u/U_{hub} at hub height. The shaded area indicates $\sigma_{u/U_{\mathrm{hub}}}$ computed using the individual measurement points of the 142 lidar scans within a certain spatial grid cell.

360   were present. The difference could be caused due to the reconstruction method using a NFoR, as the wake propagates through the scanning area causing a mismatch of the measured wind direction at the met mast and the actual wind direction at the time the wake is measured. Furthermore, the applied filtering method and the proximity to the nacelle (potentially leading to a large backscatter) could influence the captured flow field. At $0.5\,D$ the difference in the magnitude of the Gaussian minima and the Gaussian extremum is larger within the modified curled wake model in comparison to the lidar measurements, which

365   could be due to the above mentioned effects on the reconstructed wake field. At $1\,D$ the modified curled wake model better matches the measured magnitude and the position of the Gaussian minima and the Gaussian extremum. As the wake seems to

decay faster in the modified curled wake model in comparison to the field data, it could suggest that further improvement of the implemented turbulence model is needed. However, the overall comparison with the modified curled wake model shows a very good correlation with the field measurements and lies within $u/U_{\mathrm{hub}} \pm \sigma_{\mathrm{u/U_{hub}}}$, where the standard deviation is computed using the individual measurement points of the 142 scans within a certain spatial grid cell. Furthermore, the modified curled wake model provides a good estimate of the wake profile at lower wind speeds ($U_{\mathrm{hub}} = 5.6\mathrm{m/s}$).

4 Outlook to the application of the modified curled wake model

To further investigate the performance of the modified curled wake model and determine necessary future improvements, a simulation study is conducted using a turbine array consisting of five turbines in close proximity. In such a configuration the implementation of a near-wake region becomes more prevalent to accurately model the wake deficit. Differences are expected since the modified curled wake model is calibrated using a single turbine case. Furthermore, an induction model is not incorporated within the modified curled wake model and the computation of the added turbulence behind the second, third or fourth turbine does not account for the increased turbulence within the wake at the rotor. An induction model and a turbulence model accounting for the increased wake turbulence are not implemented as it is outside the scope of this paper. This section presents a comparison of the wake deficit and the power output between the 'Gaussian wake model', the 'original curled wake model' and high-fidelity simulations using a five-turbine array.

As described in Section 2, high-fidelity simulations were performed using a five-turbine array with a $2.7\,D$ spacing and three different misalignment cases. As described in Crespo et al. (1996), the added turbulence is defined as $I_+ = (I_{\mathrm{Wake}}^2 - I_0^2)^{0.5}$, where I_+ is used in Equation 9. In the current setup of the curled wake model and the modified curled wake model I_+ is computed using the free-stream turbulence intensity I_0, see Section 2.1.2, and does not account for the turbulence within the wake I_{Wake} at the waked turbines. Further consideration is needed regarding the accumulation of turbulence within a turbine array, as this determines the wake decay. One approach would be to use I_{Wake} as an input to the model proposed by Crespo et al. (1996). However, the model is determined using experimental and numerical results at the wake centre line ranging between $7\% < I_\infty < 14\%$, which is exceeded within the wake. Furthermore, the determination of the length of the near-wake region x_0 is also dependent on the turbulence at the rotor and currently uses the free-stream turbulence for each turbine. This indicates that in the current setup, the region remains similar for turbine $n \in [2,3,4,]$. The region is expected to reduce for the turbine within the wake, due to the increased turbulence level. Moreover, due to the close spacing, the wake is influenced by the induction zone of the downstream turbine. This will lead to an increase in the wake deficit within the high-fidelity simulations, not captured by the modified curled wake model or the other analytical models. As the calibration parameters were tuned for a single turbine and not for these conditions (wake being within the induction zone and an increase of the added turbulence within the wind farm) a difference in the wake deficit is expected in comparison to the high-fidelity simulations.

It can be noticed that for each case (Figure 11a -11c) the wake profile matches the high-fidelity simulations behind the first turbine, following a double-Gaussian profile. Due to the added turbulence and operating at a lower wind speed the double-Gaussian profile is less pronounced, as seen in the high-fidelity simulation, for the waked turbine. Behind the third, fourth and
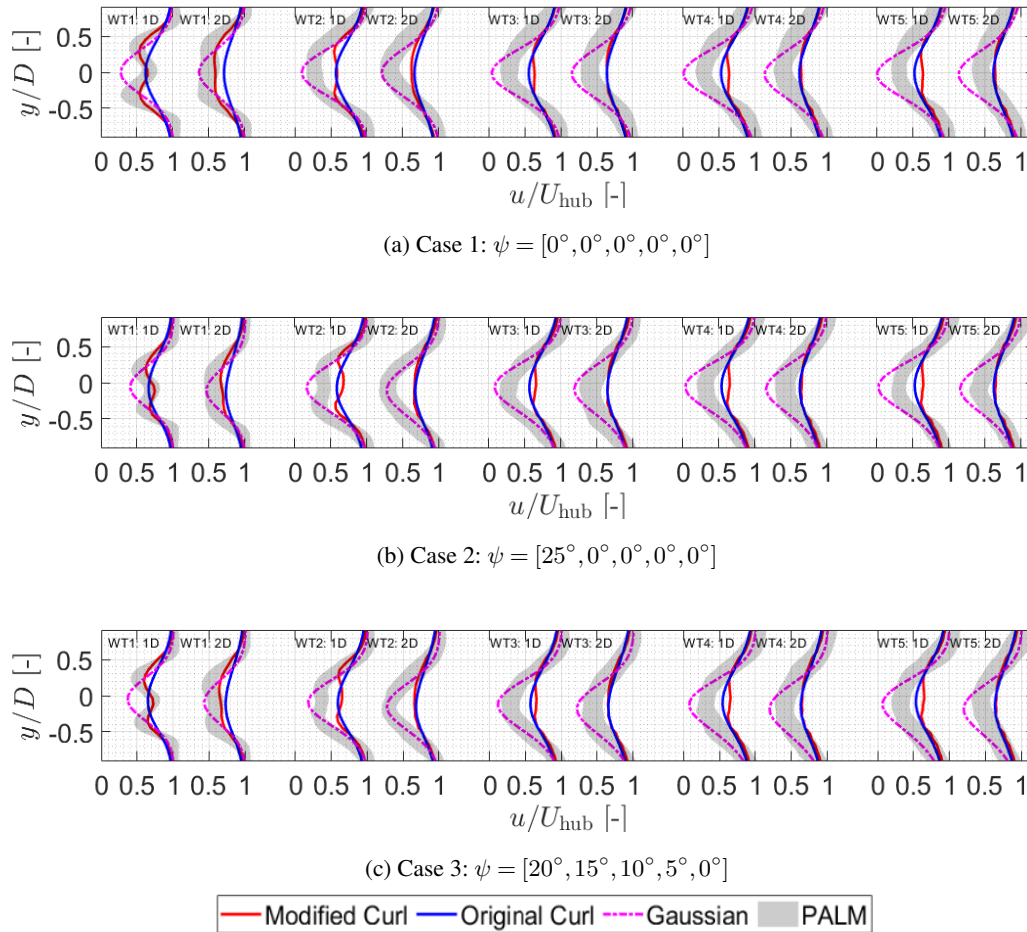
Figure 11. Comparison of the horizontal wake profile at hub height between the original curled wake model (**blue**), the modified curled wake mode l(**red**), the Gaussian wake model (**purple**) and the high-fidelity simulations (**grey**) within PALM using the horizontal wake deficit u/U_{hub} at hub height. The flow at $1\,D$ and $2\,D$ behind each turbine is shown for each case.

400 fifth turbine, the double-Gaussian profile is no longer visible, and the wake follows a Gaussian profile, which is a direct result of the accumulating turbulence within the turbine array. A similar trend is visible for the results obtained with the modified curled wake model. However, already behind the second turbine, the double-Gaussian profile is no longer visible, and a lower wake deficit is obtained in comparison to the high-fidelity simulations at $1\,D$ behind each turbine. The underestimation of the wake deficit is related to the absence of an induction zone model, as a higher local wind speed reaches the waked rotor within

405 the numerical simulation. Moreover, at a lower wind speed the double-Gaussian profile is less pronounced within the modified curled wake model, due to the drop in the thrust and with it the reduction of the wake deficit. It is expected that the added turbulence within the wake leads to a faster decay for the wake of the waked turbine, as seen in the development of the wake
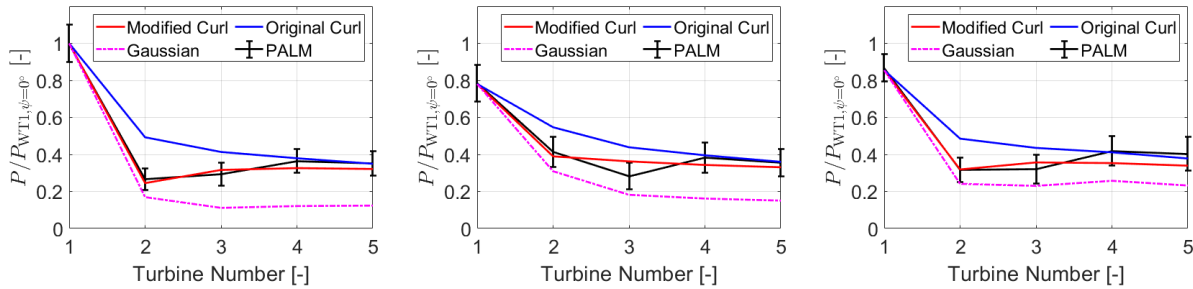
Figure 12. Comparison between the power output from various wake models and the high-fidelity simulations within PALM with $\psi = [0°, 0°, 0°, 0°, 0°]$ (**Left**), $\psi = [25°, 0°, 0°, 0°, 0°]°$ (**Centre**) and $\psi = [20°, 15°, 10°, 5°, 0°]$ (**Right**)

deficit within the numerical simulation compared to the analytically derived deficit. In Case 2 and Case 3, a double-Gaussian profile is visible due to the deflected wake of the first turbine, resulting in a lower wake deficit reaching the second turbine. For both cases, the wake follows a single-Gaussian profile after the third, fourth and fifth turbine. Similar to the analyses in Section 3.2, the Gaussian wake model does not follow the high-fidelity simulations providing a high wake deficit estimation despite not having an induction zone model. The original curled wake model also does not correspond well after the first turbine However, the profile after the third turbine resembles the modified curled wake model.

Besides analysing the computed velocity field, the power output within the turbine array is also compared (Figure 12). The power output of the modified curled wake model corresponds very well to the power output obtained from the high-fidelity simulations for each of the three simulation cases. The original curled wake model overestimates the power of the second and third turbine. This corresponds to the results in Figure 11, where the model underestimates the wake deficit. At the fourth and fifth turbine, the power output of the original curled wake model matches the power output of the modified curled wake model and the high-fidelity simulations, where the wake deficit of both models match as well, see Figure 12. The power output of the Gaussian wake model resembles the results from the high-fidelity simulations at the second turbine, but underestimates it for the third, fourth and fifth turbine for each case. The underestimation is a result of the large wake deficit computed behind the second until the fourth turbine, visible in Figure 11.

5 Conclusions

A near-wake region is implemented in the curled wake model. The implementation is done by first defining an azimuth-dependent double-Gaussian profile as an initial condition at the rotor. Five empirical parameters are tuned by high-fidelity simulations. Secondly, the turbulence model is altered to account for the difference in the turbulence decay within the near-wake region and in the far-wake region. Lastly, an estimate for the relaxation of the pressure gradient is introduced using an iterative process which accounts for the conservation of mass.

The model is tuned using high-fidelity simulations performed in PALM using an aeroelastic model of a utility turbine for the
430 misalignment angles $\psi = 0°$ and $\psi = 30°$. The numerical implementation of the near-wake region resulted in a high pressure
gradient at the rotor which decays further downstream towards zero. Additionally, the pressure gradient is set to zero at the
start of the far-wake region, as defined by Bastankhah and Porté-Agel (2016). The variation in the computed pressure field is a
direct result of the initial condition.

The computed flow field in the modified curled wake model at $\psi = 0°$ and $\psi = 30°$ correlate very well with the wake deficit
435 extracted from the high-fidelity simulations as the wake decayed further downstream. At $\psi = 0°$ an axisymmetric wake deficit
is computed, which is not the case at $\psi = 30°$ due to the azimuthal-dependent double-Gaussian profile. Furthermore, the model
showed an improvement in the computed wake deficit in the single wake case in comparison to the original curled wake model
and the Gaussian model. The wake profile showed a similar displacement of the wake 'core' in comparison to the high-fidelity
simulations and an azimuthal variation of the wake deficit at $\psi = 30°$.

440 The validation of the modified curled wake model is performed using field lidar data measuring the near-wake region.
Through reconstructing the lidar measurements using a nacelle frame of reference, a double-Gaussian profile at $0.5\,D$ and $1\,D$
is measured. The comparison of the field data and the computed wake from the modified curled wake model indicates that the
model is able to capture the wake deficit at different inflow conditions.

To determine future improvements of the modified curled wake model the performance is analysed within a turbine array
445 consisting of five turbines for three different misalignment cases. The wake deficit after the first turbine matches the wake
deficit in the high-fidelity simulations, following a double-Gaussian profile. However, after the third turbine the wake deficit
does not follow a Gaussian profile anymore and underestimates the wake deficit. This can be related to the absence of the
induction zone at the waked turbine and the accumulation of turbulence within the wake, resulting in a faster wake decay. This
indicates that further consideration is needed regarding the definition of the wake decay within a turbine array. Future work
450 should also incorporate the induction zone within the modified curled wake model to obtain a better representation of the wake
deficit within a turbine array. Despite the discrepancy in the wake deficit, the power output of the modified curled wake model
resembles the power output of the high-fidelity simulations very well for each misalignment case outperforming the original
curled wake model and the Gaussian wake model.

The implementation of the near-wake region within the curled wake model leads to a better representation of the wake deficit.
455 This will improve the definition of the optimum yaw angle to increase the power gain within a wind farm, where turbines are
positioned in close proximity, by active wake steering and advance the development of controls-oriented models.

Author contributions. PH designed the research, developed the model, conducted the measurement campaign, performed the data analysis,
prepared the figures, and planned and wrote the paper. LM and NH contributed to the development of the model, the data analysis and
the writing of the paper. MK supervised the work. All co-authors contributed with several fruitful discussions and thoroughly reviewed the
460 manuscript.

Competing interests. The authors declare that they have no conflict of interest.

Acknowledgements. This work is funded by the Federal Ministry for Economic Affairs and Energy according to a resolution by the German
Federal Parliament in the scope of the national research project "CompactWind II" (Ref. Nr. 0325492H), for which the field measurements
were carried out, and the national research project WIMS-Cluster (FKZ 0324005), through the use of computer resources. The authors would

465   like to express their gratitude to eno energy GmbH for assisting with the field experiments and providing the aeroelastic model of the turbine.
The authors would also like to acknowledge the assistance of Stephan Stone, Anantha Padmanabhan Kidambi Sekar and Jörge Schneemann
for their support during the installation of the sensors.

This work was authored in part by the National Renewable Energy Laboratory, operated by Alliance for Sustainable Energy, LLC, for the
U.S. Department of Energy (DOE) under Contract No. DE-AC36-08GO28308. Funding is provided by the U.S. Department of Energy Office

470   of Energy Efficiency and Renewable Energy Wind Energy Technologies Office. The views expressed herein do not necessarily represent
the views of the DOE or the U.S. Government. The U.S. Government retains and the publisher, by accepting the article for publication,
acknowledges that the U.S. Government retains a nonexclusive, paid-up, irrevocable, worldwide license to publish or reproduce the published
form of this work, or allow others to do so, for U.S. Government purposes.

References

475   Ainslie, J. F.: Calculating the flowfield in the wake of wind turbines, Journal of wind engineering and Industrial Aerodynamics, 27, 213–224, https://doi.org/https://doi.org/10.1016/0167-6105(88)90037-2, 1988.

Aitken, M. L., Banta, R. M., Pichugina, Y. L., and Lundquist, J. K.: Quanannoni, Journal of Atmospheric and Oceanic Technology, 31, 765–787, https://doi.org/10.1175/JTECH-D-11-00033.1, 2014.

Annoni, J., Fleming, P., Scholbrock, A., Roadman, J., Dana, S., Adcock, C., Porte-Agel, F., Raach, S., Haizmann, F., and Schlipf, D.: Analysis
480   of control-oriented wake modeling tools using lidar field results, Wind Energy Science, 3, 819–831, https://doi.org/10.5194/wes-3-819-2018, 2018.

Barthelmie, R. J., Frandsen, S. T., Nielsen, M., Pryor, S., Rethore, P.-E., and Jørgensen, H. E.: Modelling and measurements of power losses and turbulence intensity in wind turbine wakes at Middelgrunden offshore wind farm, Wind Energy: An International Journal for Progress and Applications in Wind Power Conversion Technology, 10, 517–528, https://doi.org/10.1002/we.238, 2007.

485   Bastankhah, M. and Porté-Agel, F.: A new analytical model for wind-turbine wakes, Renewable Energy, 70, 116–123, https://doi.org/10.1016/j.renene.2014.01.002, 2014.

Bastankhah, M. and Porté-Agel, F.: Experimental and theoretical study of wind turbine wakes in yawed conditions, Journal of Fluid Mechanics, 806, 506–541, https://doi.org/10.1017/jfm.2016.595, 2016.

Bay, C. J., King, J., Martìnez-Tossas, L. A., Mudafort, R., Hulsman, P., Kühn, M., and Fleming, P.: Toward flow control: An assessment
490   of the curled wake model in the FLORIS framework, in: Journal of Physics: Conference Series, vol. 1618, p. 022033, IOP Publishing, https://doi.org/10.1088/1742-6596/1618/2/022033, 2020.

Beck, H. and Kühn, M.: Dynamic data filtering of long-range Doppler LiDAR wind speed measurements, Remote Sensing, 9, 561, https://doi.org/10.3390/rs9060561, 2017.

Branlard, E., Quon, E., Forsting, A. R. M., King, J., and Moriarty, P.: Wind farm blockage effects: comparison of different engineering models,
495   in: Journal of Physics: Conference Series, vol. 1618, p. 062036, IOP Publishing, https://doi.org/10.1088/1742-6596/1618/6/062036, 2020.

Bromm, M., Vollmer, L., and Kühn, M.: Numerical investigation of wind turbine wake development in directionally sheared inflow, Wind Energy, 20, 381–395, https://doi.org/10.1002/we.2010, 2017.

Burton, T., Jenkins, N., Sharpe, D., and Bossanyi, E.: Wind energy handbook, John Wiley & Sons, 2 edn., 2011.

Conti, D., Dimitrov, N., Peña, A., and Herges, T.: Probabilistic estimation of the Dynamic Wake Meandering model parameters using
500   SpinnerLidar-derived wake characteristics, Wind Energy Science, 6, 1117–1142, https://doi.org/10.5194/wes-6-1117-2021, 2021.

Crespo, A., Hernandez, J., Fraga, E., and Andreu, C.: Experimental validation of the UPM computer code to calculate wind turbine wakes and comparison with other models, Journal of Wind Engineering and Industrial Aerodynamics, 27, 77–88, https://doi.org/10.1016/0167-6105(88)90025-6, 1988.

Crespo, A., Herna, J., et al.: Turbulence characteristics in wind-turbine wakes, Journal of wind engineering and industrial aerodynamics, 61,
505   71–85, https://doi.org/10.1016/0167-6105(95)00033-X, 1996.

Dasari, T., Wu, Y., Liu, Y., and Hong, J.: Near-wake behaviour of a utility-scale wind turbine, Journal of Fluid Mechanics, 859, 204–246, https://doi.org/10.1017/jfm.2018.779, 2019.

Drees, J. M.: A theory of airflow through rotors and its application to some helicopter problems, J. Helicopter Association of Great Britain, 3, 79–104, 1949.

510   Engelund, F. A.: Hydrodynamik, Danmarks Tekniske Højskole (Polyteknisk Boghandel), 1968.

Frandsen, S., Barthelmie, R., Pryor, S., Rathmann, O., Larsen, S., Højstrup, J., and Thøgersen, M.: Analytical modelling of wind speed deficit in large offshore wind farms, Wind Energy: An International Journal for Progress and Applications in Wind Power Conversion Technology, 9, 39–53, https://doi.org/10.1002/we.189, 2006.

Hamilton, N.: Atmospheric condition identification in multivariate data through a metric for total variation, Atmospheric Measurement Techniques, 13, 1019–1032, https://doi.org/10.5194/amt-13-1019-2020, 2020.

Hamilton, N., Bay, C. J., Fleming, P., King, J., and Martínez-Tossas, L. A.: Comparison of modular analytical wake models to the Lillgrund wind plant, Journal of Renewable and Sustainable Energy, 12, 053 311, https://doi.org/10.1063/5.0018695, 2020.

Howland, M. F., Bossuyt, J., Martinez-Tossas, L. A., Meyers, J., and Meneveau, C.: Wake Structure of Wind Turbines in Yaw under Uniform Inflow Conditions, arXiv preprint arXiv:1603.06632, https://doi.org/10.48550/arXiv.1603.06632, 2016.

Hu, H., Yang, Z., and Sarkar, P.: Dynamic wind loads and wake characteristics of a wind turbine model in an atmospheric boundary layer wind, Experiments in fluids, 52, 1277–1294, https://doi.org/doi.org/10.1007, 2012.

Hulsman, P., Wosnik, M., Petrović, V., Hölling, M., and Kühn, M.: Development of a curled wake of a yawed wind turbine under turbulent and sheared inflow, Wind Energy Science, 7, 237–257, https://doi.org/10.5194/wes-7-237-2022, 2022.

Iungo, G. V., Wu, Y.-T., and Porté-Agel, F.: Field measurements of wind turbine wakes with lidars, Journal of Atmospheric and Oceanic Technology, 30, 274–287, https://doi.org/10.1175/JTECH-D-12-00051.1, 2013.

Jensen, N. O.: A note on wind generator interaction, Risø National Laboratory, Risø-M No. 2411, 1983.

Jonkman, J. M., Buhl Jr, M. L., et al.: FAST user's guide, National Renewable Energy Laboratory, Golden, CO, Technical Report No. NREL/EL-500-38230, 2005.

Keane, A., Aguirre, P. E. O., Ferchland, H., Clive, P., and Gallacher, D.: An analytical model for a full wind turbine wake, Journal of Physics: Conference Series, 753, 032 039, https://doi.org/10.1088/1742-6596/753/3/032039, 2016.

Krüger, S., Steinfeld, G., Kraft, M., and Lukassen, L. J.: Validation of a coupled atmospheric–aeroelastic model system for wind turbine power and load calculations, Wind Energy Science, 7, 323–344, https://doi.org/10.5194/wes-7-323-2022, 2022.

Larsen, G. C., Højstrup, J., and Madsen, H. A.: Wind fields in wakes, European Union wind energy conference. Proceedings (pp. 764-768), 1996.

Larsen, G. C., Madsen, H. A., Thomsen, K., and Larsen, T. J.: Wake meandering: a pragmatic approach, Wind energy, 11, 377–395, https://doi.org/10.1002/we.267, 2008.

Madsen, M. H. A., Zahle, F., Sørensen, N. N., and Martins, J. R.: Multipoint high-fidelity CFD-based aerodynamic shape optimization of a 10 MW wind turbine, Wind Energy Science, 4, 163–192, https://doi.org/10.5194/wes-4-163-2019, 2019.

Magnusson, M.: Near-wake behaviour of wind turbines, Journal of Wind Engineering and Industrial Aerodynamics, 80, 147–167, https://doi.org/10.1016/S0167-6105(98)00125-1, 1999.

Maronga, B., Gryschka, M., Heinze, R., Hoffmann, F., Kanani-Sühring, F., Keck, M., Ketelsen, K., Letzel, M. O., Sühring, M., and Raasch, S.: The Parallelized Large-Eddy Simulation Model (PALM) version 4.0 for atmospheric and oceanic flows: model formulation, recent developments, and future perspectives, Geoscientific Model Development, 8, 2515–2551, https://doi.org/10.5194/gmd-8-2515-2015, 2015.

Martínez-Tossas, L. A., Annoni, J., Fleming, P. A., and Churchfield, M. J.: The aerodynamics of the curled wake: a simplified model in view of flow control, Wind Energy Science, 4, 127–138, https://doi.org/10.5194/wes-4-127-2019, 2019.

Neunaber, I., Hölling, M., Stevens, R. J., Schepers, G., and Peinke, J.: Distinct turbulent regions in the wake of a wind turbine and their inflow-dependent locations: the creation of a wake map, Energies, 13, 5392, 2020.

Nilsson, K., Ivanell, S., Hansen, K. S., Mikkelsen, R., Sørensen, J. N., Breton, S.-P., and Henningson, D.: Large-eddy simulations of the Lillgrund wind farm, Wind Energy, 18, 449–467, https://doi.org/10.1002/we.1707, 2015.

550 Qian, G.-W. and Ishihara, T.: A new analytical wake model for yawed wind turbines, Energies, 11, 665, https://doi.org/10.3390/en11030665, 2018.

Ronsten, G.: Static pressure measurements on a rotating and a non-rotating 2.375 m wind turbine blade. Comparison with 2D calculations, Journal of Wind Engineering and Industrial Aerodynamics, 39, 105–118, https://doi.org/10.1016/0167-6105(92)90537-K, 1992.

Sanderse, B.: Aerodynamics of wind turbine wakes, Energy Research Center of the Netherlands (ECN), ECN-E–09-016, Petten, The Nether-
555 lands, Tech. Rep, 5, 153, 2009.

Schreiber, J., Balbaa, A., and Bottasso, C. L.: Brief communication: A double-Gaussian wake model, Wind Energy Science, 5, 237–244, https://doi.org/10.5194/wes-5-237-2020, 2020.

Snel, H. and Schepers, J. G.: Joint investigation of dynamic inflow effects and implementation of an engineering method, Technical Report ECN-C-94-107, Netherlands Energy Research Foundation (ECN), Petten (Netherlands), 1995.

560 Vermeer, L., Sørensen, J. N., and Crespo, A.: Wind turbine wake aerodynamics, Progress in aerospace sciences, 39, 467–510, https://doi.org/10.1016/S0376-0421(03)00078-2, 2003.

Zhang, W., Markfort, C. D., and Porté-Agel, F.: Near-wake flow structure downwind of a wind turbine in a turbulent boundary layer, Experiments in fluids, 52, 1219–1235, https://doi.org/10.1007/s00348-011-1250-8, 2012.